Composites Part A 116 (2019) 216–223

Contents lists available at ScienceDirect

Composites Part A

journal homepage: www.elsevier.com/locate/compositesa

In situ analysis of interfacial damage in adhesively bonded composite joints subjected to various surface pretreatments

Ran Tao[a], Marco Alfano[b], Gilles Lubineau[a,*]

[a] King Abdullah University of Science and Technology (KAUST), Physical Sciences and Engineering Division (PSE), COHMAS Laboratory, Thuwal 23955-6900, Saudi Arabia

[b] Department of Mechanical, Energy and Management Engineering, University of Calabria, 87036 Rende (CS), Italy

ARTICLE INFO

Keywords:
A. Laminates
E. Joints/joining
E. Surface treatments
E. Laser

ABSTRACT

Secondary bonding of carbon fiber-reinforced polymer (CFRP) using structural adhesives is a promising technology. However, the joint performance can be ultimately affected by surface modifications attained through different surface preparation strategies. Thus, there is still a need for experimental techniques capable of assessing the mechanical properties associated with different surface preparations, and their relation to the damage morphology at initiation. In this work, a refined experimental set-up was used to perform three-point bending tests on miniaturized single-lap composite joints. Such testing configuration features a peel-dominant stress field within the bondline and the possibility to track the evolution of adhesive deformation and damage *in situ* at the meso-scale using optical microscopy. Epoxy-bonded CFRP joints were evaluated as a function of various surface pretreatments. *In situ* local observation obtained during mechanical loading provided insights into the detailed mechanisms taking place depending on the surface preparation strategies.

1. Introduction

Lightweight materials continue to gain increasing importance within the aerospace and automotive industries due to growing demand for emissions reduction and resource efficiency. Carbon fiber-reinforced polymers (CFRPs) have been widely adopted by the aviation industries to reduce fuel consumption and increase the passenger/cargo load, such as the fuselage, wings, fan blades, and tail cones of the Boeing Dreamliner 787 (2011) and the Airbus A350X (2014) [1]. The increasing use of CFRPs for commercial products requires fast and reliable methods for structural assemblage. To date, joining is still a major cost source. Conventional mechanical fastenings, using rivets or bolts, are not ideal for joining CFRPs because substrate drilling and fastener installation [2] require expensive labor and rework, increase the total weight, induce stress concentration, and cause undesired fiber breakage.

Thanks to recent developments in structural adhesives and advanced surface preparation techniques [3–6], secondary adhesive bonding has the potential to join cured composite laminates without the use of rivets and bolts. The most important concern regarding secondary bonding is that an additional surface preparation step is mandatory to ensure the joint performance and safety. Classical surface pretreatments for cured composite laminates include a variety of techniques, such as sanding, sandblasting, and the use of peel-ply [7,8]. Sanding, as well as sandblasting, have been used for a very long time because they can efficiently remove surface contamination, increase contact area and, as a result, the joint strength. But such treatments introduce dust pollution to the working environment, are mostly operator-dependent, and induce damage to surface fibers. As an alternative, the use of peel-ply is often preferred. The peel-ply absorbs excess resin material during curing, and the subsequent removal should be able to generate a fresh active surface through polymer chain scission. Unfortunately, peel-plies may also have a weak interaction with the laminate and after removal defected imprinted texture, with non-uniformly distributed contaminants, is usually found on the composite surfaces [8,9]. Therefore, classical sanding and peel-ply treatments frequently deliver variable mechanical responses.

Current manufacturing developments are now focusing on highly controllable and reproducible processes, which aim to reduce the contamination and/or process variation. Pulsed lasers are very promising since they are environmentally friendly, suitable for large-scale applications, and able to efficiently remove the contaminated resin layer inducing little or no damage on surface fibers [9–13]. Current lasers employed to treat CFRPs operate at wavelengths ranging from UV [11,12,14,15] to IR [16,17] range, and modify the target materials differently [18,19]. IR lasers, such as CO_2 lasers, induce photothermal

* Corresponding author.
E-mail addresses: marco.alfano@unical.it (M. Alfano), gilles.lubineau@kaust.edu.sa (G. Lubineau).

https://doi.org/10.1016/j.compositesa.2018.10.033
Received 24 June 2018; Received in revised form 19 October 2018; Accepted 24 October 2018
Available online 25 October 2018
1359-835X/

surface modifications, thereby depositing more heat on the surface and increasing the risk of damage and delamination of CFRP surface layers. However, the high processing speed and area rate of treated material renders CO_2 lasers good candidates for large-scale industrial applications [18].

Various surface preparation techniques employed for CFRPs can result in different surface modifications which play a fundamental role in the damage at initiation and ultimately on the joint strength. Thus, a careful assessment of the failure process at the relevant length scale is highly desirable to qualify a surface pretreatment for a given material system. *In situ* local observations of the bondline under loading could allow to better understanding the interaction between formation and evolution of damage across the interface and surface properties of the composite (*e. g.*, topography and material composition).

To this purpose, a dedicated experimental set-up is deployed in this work, which comprised a miniaturized tensile stage and a high-resolution microscope coupled with a high-speed camera. The test coupon utilized in the experiments is a standard single-lap joint (SLJ) [20] comprising aerospace grade CFRP adherends. The sample is subjected to out-of-plane loading conditions, *i. e.*, three-point bending [21]. It has been shown that this particular configuration is characterized by a peel-dominant stress field within the bondline and enables relatively easy access to the small-scale *in situ* damage processes within the bondline [22]. The manuscript is organized as follows. First, surface pretreatments are outlined. Then, the resulting surface topography and energy were characterized through a wide range of techniques, including surface profilometry, high-resolution electron microscopy, and the sessile drop technique in conjunction with the Owens-Wendt theory. Adhesive joints with CFRP laminates were fabricated and tested in the single-lap configurations loaded under three-point bending. The localized damage mechanisms were ascertained at the meso-scale through *in situ* high-resolution observations assisted by a high-speed camera. This combined analysis, including both morphological and *in situ* mechanical characterizations, provided new insights into the damage mechanisms taking place depending on the surface preparation strategies.

2. Materials and methods

2.1. Material

The substrates were made with eight-layer unidirectional CFRP prepregs (HexPly T700/M21, Hexcel, Stamford, CT, USA), and the adhesive was two-component epoxy (Araldite 420 A/B, Huntsman, Salt Lake City, UT, USA). The detailed material properties and fabrication process were already reported in the authors' previous work [9]. The surface energy of the selected adhesive was obtained through two sequential tests. First, the total surface energy of the liquid (l) in a vapor atmosphere (v) γ_{lv} was obtained using a force tensiometer (K100, KRUESS, Hamburg, Germany). By pulling the probe plate at a speed of 10 mm/min, the averaged surface energy was obtained as $\gamma_{lv} = 30.7$ mN/m. Then, the mixed adhesive paste was dropped onto a pure dispersive Teflon surface (PTFE) and the corresponding contact angle was measured to obtain the dispersive and polar components of surface energy as $\gamma_{lv}^{d} = 17.7$ mN/m, $\gamma_{lv}^{p} = 13.0$ mN/m.

2.2. Surface pretreatments

Three surface conditions were investigated in this study. A nominally flat surface, named *T*, was obtained by covering the surface of the pre-preg stack with a Teflon film, which was removed after curing. Sanding, a conventional mechanical abrasion technique was performed on the *T* surfaces to increase the adhesive/CFRP contact surface and, thus, to enhance the adhesion. The sanding was carried out using a grinding and polishing machine (Tegra Force-5, Struers, OH, USA), and the CFRP laminates were held manually for 5 min on 320-grit sandpaper under a rotation speed of 300 rpm to obtain a uniform sanded surface, called *S*. Pulsed CO_2 laser irradiation ($\lambda = 10.6$ μm, PLS6.75 Laser Platform, Universal Laser Systems, NY, USA) was carried out as the third pretreatment technique. The process parameters were carefully set up, based on investigations carried out by the authors, to enable a reasonably fast and uniform surface treatment [9]. In this work, a pulse fluence equal to $F_p = 1.2$ J/cm^2 was adopted (*LC*, Table 1), in order to lightly evaporate the surface matrix of the laminate. The nominal flat Teflon surface was considered as the baseline condition since both *S* and *LC* surface pretreatments were carried out on *T* surfaces. Apart from the aforementioned surface pretreatments, *T*, *S*, and *LC*, another batch of specimens was prepared using a classical polyamide peel-ply (Diatex PA85, Diatex, Saint Genis Laval, France), which was laminated on the pre-preg stack. Since it is a very common surface condition encountered in industrial practice, the peel-ply-treated surfaces will be used for comparative analysis and denoted as *PP* in this work.

Table 1
Processing parameters of the CO_2 laser.

Process parameters	Value
Laser wavelength (μm)	10.6
Spot diameter (μm)	200
Laser speed (mm/s)	500
Pulse frequency (kHz)	20
Average power (W)	7.5
Processing gas (–)	Air

Finally, all the surfaces were degreased in an ultrasonic bath of acetone for 10 min and then oven dried at 50 °C for 25 min before adhesive bonding to remove any residual contamination associated with the laminate cutting and handling.

2.3. Surface profilometry

3D optical surface profiler (Zygo NewView 7300 Optical Surface Profiler, Lambda Photometrics, Harpenden, UK) was used to reveal the micro-scale surface topography. The treated surfaces were coated with a thin Au layer (25 nm) using a high-resolution sputter coater (Cressington 208HR, Cressington Scientific Instruments, Watford, UK) to improve the accuracy of the measurements. The observation field-of-view was 350 μm × 260 μm by using a 20× optical lens. At the meso-scale, scanning electron microscopy (SEM, Quanta 600, FEI, CA, USA) with secondary electron imaging was deployed to resolve the morphological features generated by the various pretreatments. Furthermore, macro-scale surface profiles of the treated surfaces were assessed using contact profilometry (Dektak 150 Surface Profiler, Veeco, New York, USA) with the same gauge length (3 mm) and sampling resolution (0.1667 μm/point) as the authors' previous work [9]. The area roughness S_a was estimated by averaging the line roughness R_a obtained in both the parallel (x-) and perpendicular (y-) directions, *i. e.*, $S_a = \frac{R_{ax} + R_{ay}}{2}$.

2.4. Sessile drop technique and wetting envelopes

When a liquid droplet makes contact with a solid surface, it forms a specific shape representing the stable thermodynamics energy of the solid(s)-liquid(l)-vapor(v) system (Fig. 1(a)). Based on the Young's equation and the Owens-Wendt theory, thermodynamic equilibrium of the solid surface energy γ_{sv} and the liquid surface energy γ_{lv} can be described by the following relationship [23]:

$$\frac{\gamma_{lv}(cos\theta + 1)}{2\sqrt{\gamma_{lv}^{d}}} = \frac{\sqrt{\gamma_{lv}^{p}}}{\sqrt{\gamma_{lv}^{d}}}\sqrt{\gamma_{sv}^{p}} + \sqrt{\gamma_{sv}^{d}}, \quad (1)$$

where θ is the contact angle between the vapor/liquid interface and the liquid/solid interface at the contact contour (Fig. 1(a)), while d and p

(a)

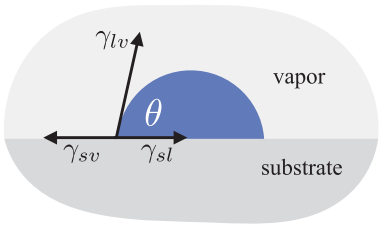

Test liquids	γ^{d}_{lv}	γ^{p}_{lv}	γ_{lv}
formamide	39	19	58
ethylene glycol	29	19	48
deionized water	22	51	73

(b)

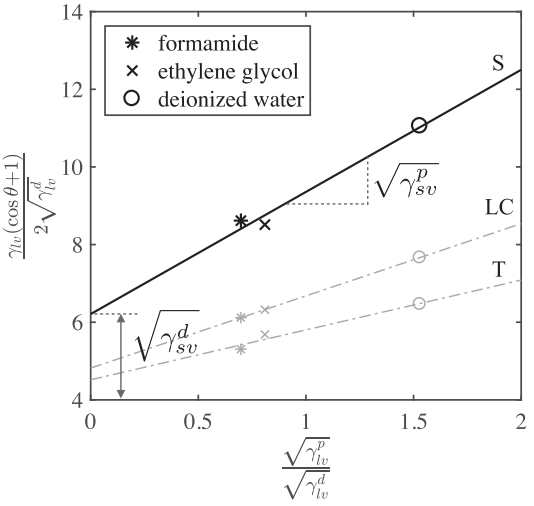

Fig. 1. (a) Schematic of a sessile liquid drop (l) placed on a solid surface (s) in the presence of vapor (v). The table provides the dispersive component γ^d_{lv}, the polar component γ^p_{lv}, and the total surface energy γ_{lv} of the selected liquids. The surface energies are given in [mN/m]. (b) The determination of the surface energy based on the Owens-Wendt theory in conjunction with contact angle measurements of *T*, *LC*, and *S* surfaces analyzed in this study. (For interpretation of the references to color in this figure legend, the reader is referred to the web version of this article.)

represent the dispersive and polar components of the surface energy, respectively. According to the Owens-Wendt theory, the dispersive and the polar component of the surface energy satisfy the following relation: $\gamma_{lv} = \gamma^d_{lv} + \gamma^p_{lv}$ for liquid, and $\gamma_{sv} = \gamma^d_{sv} + \gamma^p_{sv}$ for solid.

The surface energy was assessed by the sessile drop technique by applying multiple known liquids to the solid substrate and measuring the corresponding contact angles. The measurement was conducted at room temperature and ambient pressure in a class 1000 (ISO 6) cleanroom using a drop shape analyzer (DSA 100, KRUESS, Hamburg, Germany). Three testing liquids, formamide, ethylene glycol, and deionized water, were employed in the measurement. The surface energies of the test liquids and the corresponding $(\frac{\sqrt{\gamma^p_{lv}}}{\sqrt{\gamma^d_{lv}}};\frac{\gamma_{lv}(\cos\theta+1)}{2\sqrt{\gamma^d_{lv}}})$ data points obtained experimentally for the investigated surfaces (*T*, *LC*, and *S*) are reported in Fig. 1. At least five contact angle measurements were performed, and the volume of the droplet was well controlled at 4 μL. Measurements were made both parallel and perpendicular to the fiber orientation. The dispersive and polar components of surface energies were finally obtained using the intercept and the slope of the linear interpolation plot of the above data points, as plotted in Fig. 1(b).

Then, wetting envelopes were determined. Assuming that the liquid could perfectly wet the surface, the γ^p_{lv} versus γ^d_{lv} plot was obtained with respect to a certain solid surface. By setting $\theta = 0°$ in Eq. (1), one obtains:

$$\gamma^p_{lv} - \sqrt{\gamma^p_{sv}\gamma^p_{lv}} + \gamma^d_{lv} - \sqrt{\gamma^d_{sv}\gamma^d_{lv}} = 0, \quad (2)$$

which represents a contour of the constant equilibrium contact angle ($\theta = 0°$) of the investigated solid surface (*i. e.*, the wetting envelope). Liquids with surface energy components that lie outside the γ^p_{lv}-γ^d_{lv} contour will not wet the investigated surface completely. Thus, the obtained wetting envelope allows qualitative wettability assessment of the solid surface.

2.5. Fabrication of single-lap joints and mechanical set-up

Three-point bending tests were carried out using the SLJ configuration. CFRP laminates ($[0°]_8$) were cut into 50 × 24 × 2 mm^3 strips and then bonded using the epoxy adhesive with an overlap length of 8 mm. A schematic depiction of the laminate assembly is given in Fig. 2(a). Two copper wires with 100 μm diameters were used as well as mechanical pressure to ensure a controlled and constant thickness of the adhesive layer. The joints were cured in a temperature- and moisture-controlled environment, *i. e.*, 21 °C and 55% R.H., for 12 h. Then, the bonded plate was cut into 6 mm width slices and both sides of the slice were polished to eliminate the surface flaws before the miniature bending tests (Fig. 2(b)). The adhesive thicknesses of the SLJs were measured at three different locations on both sides. The results showed that the fabrication was consistent; the adhesive thicknesses were equal to 94.2 ± 0.8 μm (*PP*), 104.3 ± 4.1 μm (*T*), 96.2 ± 3.6 μm (*LC*), and 96.3 ± 4.7 μm (*S*).

Mechanical tests were performed using a micro-tensile stage (Tensile/Compression Module, Krammrath & Weiss, Dotmund, Germany) with a 1 kN load cell. The loading was under displacement control at a speed of 0.5 μm/s. A schematic depiction of the loading and boundary conditions is given in Fig. 2(c). At least five specimens of each surface pretreatment were continuously loaded till the final failure. *In situ* observations of the interfacial damage evolution were obtained using a high-resolution microscope (SteREO Discovery V20, Carl Zeiss, Oberkochen, Germany) coupled with a high-speed camera (Fastcam SA3, Photron, Tokyo, Japan) with a frame rate of 125 fps. Secondary electron imaging of SEM was employed to probe the fracture surfaces after testing and unravel the mechanisms of failure.

3. Results and discussion

3.1. Surface topography

Micro- and meso-scale observations of the surface topography after the various pretreatments are shown in Fig. 3, where *x*- is the fiber direction. The SEM images of meso-scale surface topography did not display significant anisotropy in any of the tested surfaces, which was also supported by the scanned profiles where the average roughness was similar in two orthogonal directions ($R_{ax} = R_{ay}$). The baseline *T* surface displayed carbon fibers on the 3D topography map, indicating a very thin surface epoxy layer, and the imprinted texture of the Teflon film was observed on the SEM image. The macroscale roughness of the baseline surface was relatively low, *i. e.*, $S_a = (3.06 \pm 0.84)$ μm. After pulsed laser irradiation, *LC*, the surface roughness was slightly increased to $S_a = (4.17 \pm 0.94)$ μm because of the removal of the surface resin and the partially exposed fibers, as shown in the 3D topography maps and the SEM images. This may play a relevant role in the development of the interfacial damage during mechanical tests. Sanding flattened the CFRP surface, and the S_a decreased sharply to $S_a = (0.43 \pm 0.10)$ μm, *i. e.*, was one order of magnitude lower than that

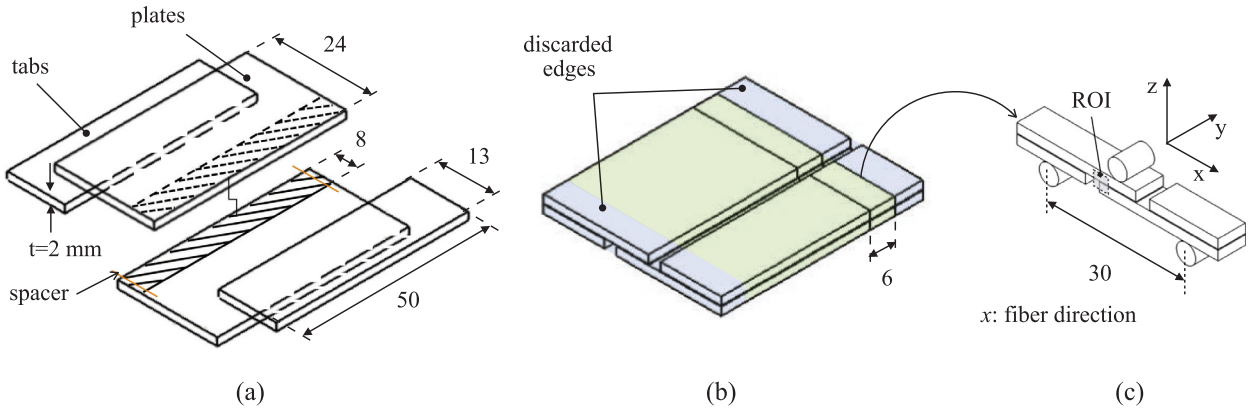

Fig. 2. Main processing steps related to fabrication and testing of single-lap joints. (a) Assembly and bonding of plates and tabs; (b) curing and cutting of plates; and (c) mechanical testing under three-point bending. The region of interest (ROI) is at the left edge of the overlap region. The quoted dimensions are given in [mm]. (For interpretation of the references to color in this figure legend, the reader is referred to the web version of this article.)

recorded on the baseline *T* surface. The blue regions in the 3D profile map represent very deep surface cavities associated with the fiber removal. In summary, both *LC* and *S* removed the surface resin and exposed carbon fibers, and the corresponding effect on surface energy will be discussed next.

3.2. Surface energy and wetting envelope

Surface energies were obtained using the average contact angles of formamide, ethylene glycol, and deionized water on the solid surfaces, which are reported in Table 2. All three surfaces maintained the higher dispersive character of the baseline *T* surface. Both *LC* and *S* improved γ_{sv}^{d} and γ_{sv}^{p}, indicating potential enhancement of adhesion at the adhesive/CFRP interfaces. Wetting envelopes corresponding to $\theta = 0°$ and $\theta = 90°$ are shown in Fig. 4, and typical droplets of deionized water on the selected surfaces are also shown in the insert. The liquids inside the envelope contour of $\theta = 0°$ completely wet the surface. Thus, the sanded surface featured the highest wettability among the considered surface pretreatments. Laser cleaning led to better wettability than the baseline *T*, but the improvement was not as prominent as that of *S*. The surface energy of applied Araldite 420 liquid adhesive was located between the contours of $\theta = 0°$ and $\theta = 90°$ for both *T* and *LC*.

Table 2
Dispersive γ_{sv}^{d}, polar γ_{sv}^{p}, and total surface energy γ_{sv} of investigated *T*, *LC*, and *S* surfaces.

Surface	Dispersive (mN/m)	Polar (mN/m)	Total (mN/m)
T	20.42	1.65	22.07
LC	23.21	3.46	26.67
S	38.59	9.88	48.47

Therefore, it partially wet the baseline and laser-treated surfaces, while it completely wet on the sanded surfaces (Fig. 4).

Previously, the authors found that *LC* partially removed surface contaminants and activated surface polar groups [9]. Thus, laser-treated surfaces enhanced the surface energy, but the obtained surface energy was still lower than that of *S*. To achieve a wettability comparable to the sanding pretreatment, further assessment was conducted by performing *LC* multiple times. However, the resulting contact angles of deionized water on the treated surfaces only slightly decreased. Moreover, this multi-step treatment exposed more loose carbon fibers, which made the contact contour of the droplet no longer circular. This effect led to an inaccurate estimation of the surface energy; moreover,

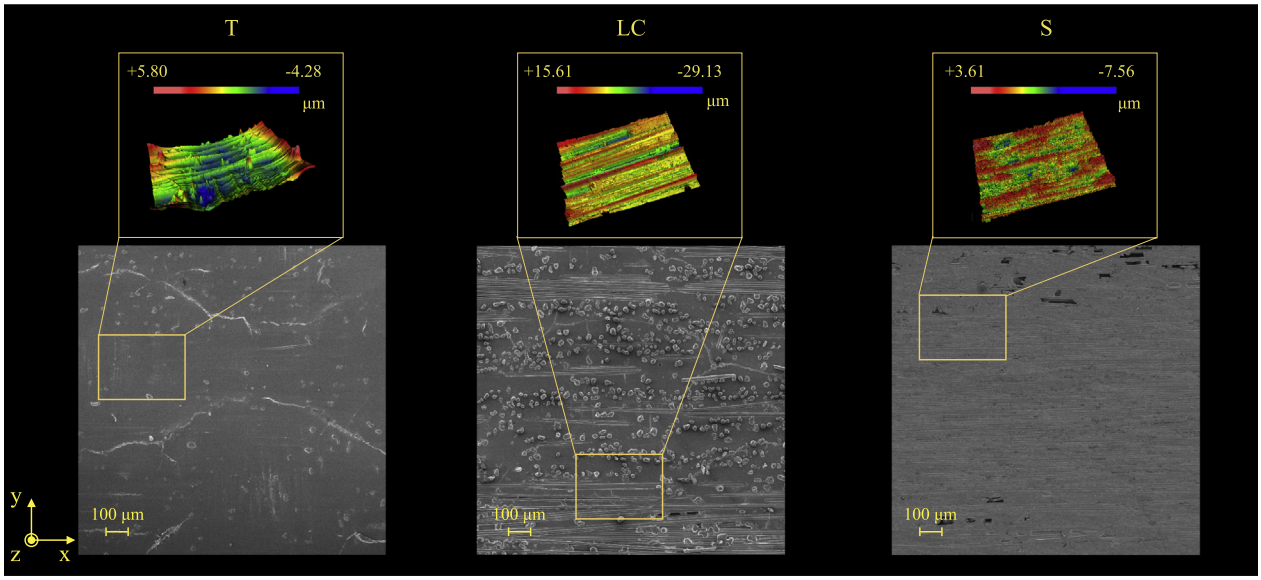

Fig. 3. Surface profilometry and scanning electron microscopy of selected surfaces. Topography maps were obtained from a 3D optical profiler. The inserted yellow boxes show the representative size of the 3D topography maps. (For interpretation of the references to color in this figure legend, the reader is referred to the web version of this article.)

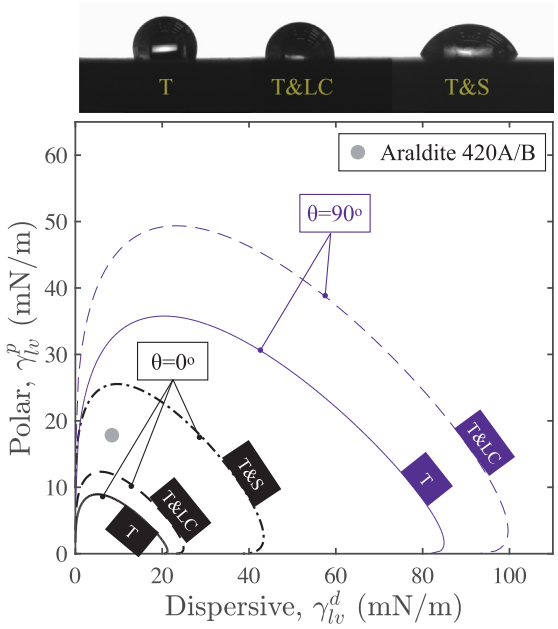

Fig. 4. Wetting envelopes of $\theta = 0°$ and $\theta = 90°$ pertaining to selected surfaces. The surface energy of Araldite 420 epoxy adhesive is represented by the gray circle, and was measured using a force tensiometer. The inserts show representative liquid drops of deionized water on the analyzed surfaces. (For interpretation of the references to color in this figure legend, the reader is referred to the web version of this article.)

an excess of loose carbon fiber does not improve adhesion [9].

3.3. Results of three-point bending tests

The load-displacement responses of *T*, *LC*, and *S* recorded during three-point bending tests are reported in Fig. 5(a). The responses consist of an initial linear elastic region, which corresponds to the bending of the SLJs, followed by a non-linear response, and sudden failure. The initial point of the non-linear response was defined by a 5% offset of the linear slope, as shown in the plots. The *PP* global response is also reported in Fig. 5(a) for comparison. All the *T*, *LC*, and *S* surfaces clearly reached higher maximum loads and final displacements than the *PP* surfaces, indicating that they all outperformed the conventional peel-ply preparation strategy. The laser-treated (*LC*) specimens achieved a higher maximum load and displacement than the baseline (*T*) ones, while the sanded (*S*) specimens had the best mechanical response among three investigated pretreatments. Laser-treated and baseline SLJ specimens had a similar region of non-linear response, while on *S* surfaces it was more extended.

Bar plots summarizing the maximum load and total surface energy as a function of the various surface pretreatments are reported in Fig. 5(b). The maximum load increased from *T* to *S* almost linearly. In particular, *T* was 41% higher than that of *PP*, while *LC* and *S* were 62% and 89% higher, respectively. The results illustrated a good correlation between the maximum load and the surface energy. On the other hand, given that the area roughness of *PP* was $S_a = 12.56$ μm, the maximum load of the three-point bending tests was not correlated with the increase of surface roughness. This is consistent with previous works on the subject which highlighted that an increase in surface roughness does not bear guarantee of improved adhesion [8,24,25]. The mechanisms behind the observed mechanical responses are assessed further in what follows.

3.4. In situ local observations of the interfacial damage

In situ optical observations were employed to investigate the failure mechanisms of SLJs. Typical observations of the interfacial damage on the various treated surfaces are shown in Fig. 6. The snapshots were extracted from the region highlighted by arrows in the global responses in Fig. 5. The total time elapsed between the first and last image was 40 s. The analysis of the snapshots did not reveal any significant displacement in the x-direction (shear) at the marked positions, which supports a peel-dominated strain (and stress) field within the adhesive layer, as already pointed out by a previous study [22]. In order to track the deformation sustained in the adhesive layer, the final maximum residual thickness (Δ_s^f) was recorded at the marked positions, as shown in Fig. 6.

The peel-ply texture imprinted on CFRP substrate led to a very rough *PP* surface ($S_a = 12.56$ μm); therefore, a large geometrical variation across the thickness of the adhesive layer can be observed in Fig. 6. Despite the roughness S_a of the *PP* surface, the interfacial damage occurred during the early stage of loading and thus resulting in

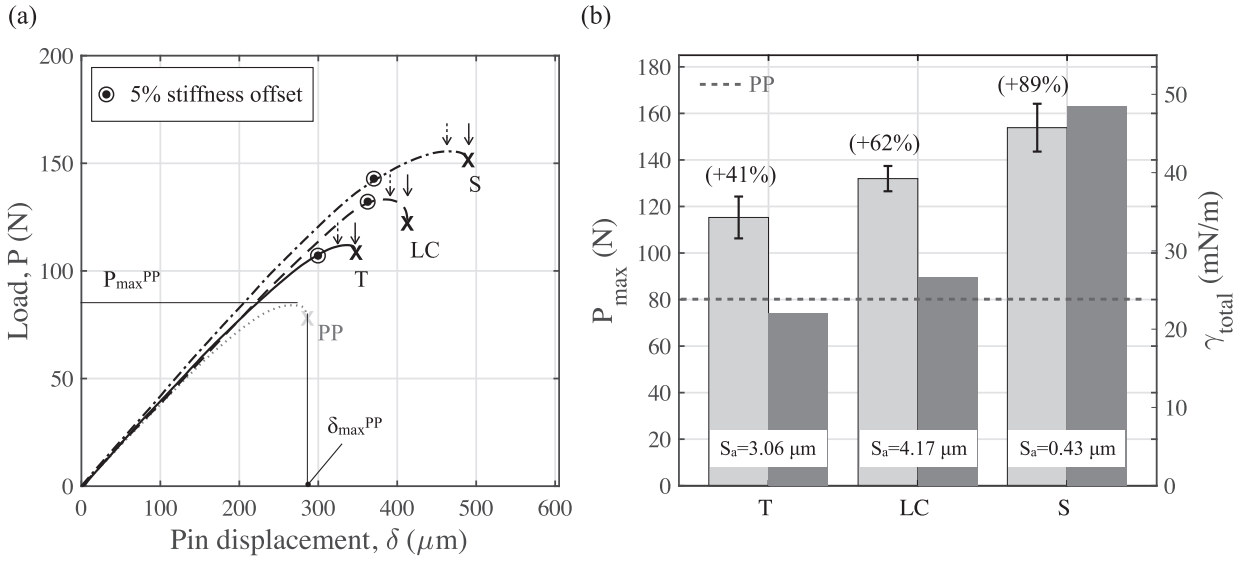

Fig. 5. (a) Typical experimental load-displacement curves of *T*, *LC*, and *S*. (b) Maximum global loads and total surface energies of investigated surfaces. Corresponding average surface roughnesses S_a of tested surfaces are displayed in the chart. The dashed line is the average maximum load of *PP* surfaces. The relative increases in maximum load compared to *PP* are shown in parenthesis.

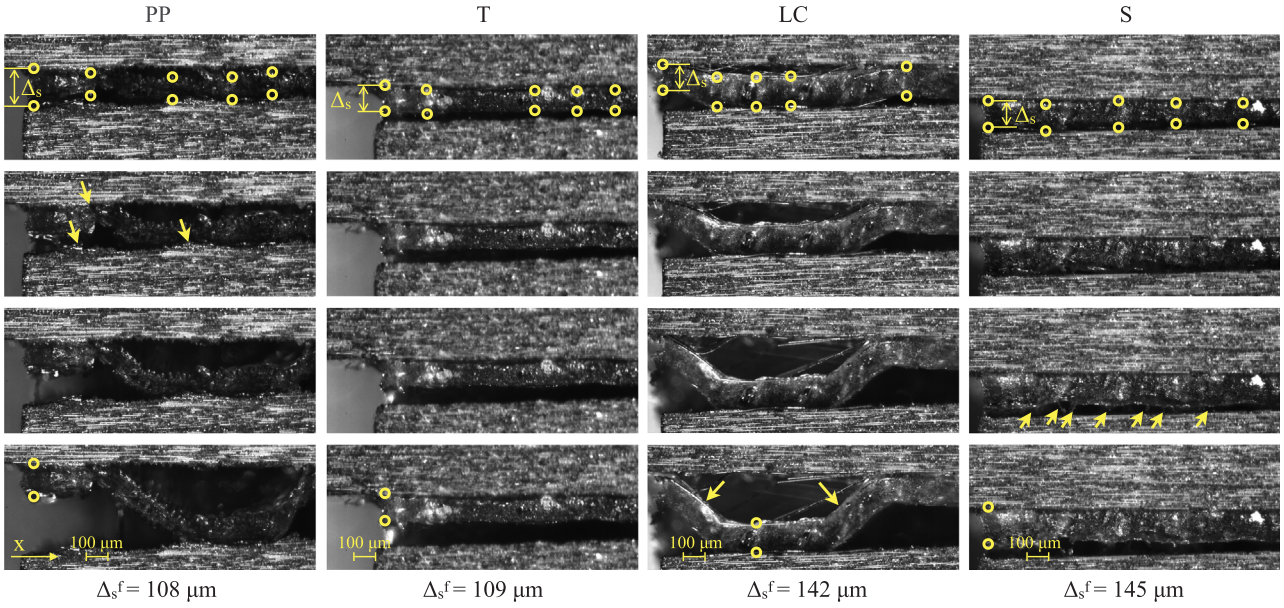

Fig. 6. *In situ.* snapshots of the interfacial damage evolution of different surface pretreatments. The evolution of the local adhesive residual thickness (Δ_s) is tracked by the circular markers. The text box provides the final residual thickness instantly before final failure (Δ_s^f). The damage progresses from top to bottom with the total time period of 40 s. (For interpretation of the references to color in this figure legend, the reader is referred to the web version of this article.)

the lowest maximum load, as shown in the corresponding global response. Local analyses, shown in Fig. 6, indicated that the adhesive layer progressively detached from both top and bottom adhesive/CFRP interfaces, revealing weak interfacial interaction. Occasionally, the detached layer bridged the CFRP surfaces at the edges of the peel-ply texture,[1] as illustrated by the arrows. Because of the weak adhesion, the residual Δ_s^f recorded during the tests was very low, implying that very little deformation was absorbed by the adhesive layer prior to fracture.

The baseline *T* was less rough but showed a slightly better mechanical response than *PP*. The detachment of the adhesive layer was mainly localized to one adhesive/CFRP interface, with limited adhesive peel deformation (Δ_s^f = 109 μm). SEM imaging of the fracture surface (Fig. 7) confirmed the local observations since mainly interfacial failure was observed.

Both subsequent surface pretreatments, *LC* and *S*, enhanced the maximum load and promoted the peel deformation of the adhesive layer, but the failure configurations were very different (Fig. 6). In *LC* specimens, near-interfacial debonding was initiated at locations featuring abundant loose fibers. Carbon fibers pulled out from the CFRP substrate were also observed on SEM fracture surface (pointed by the arrows in Fig. 7), which led to mixed failure. Spots of cohesive failure were also found on the fracture surface where no fibers were exposed. The adhesive layer detached from both top and bottom adhesive/CFRP interfaces because the randomly distributed exposed fibers prevented localization of the interfacial damage and triggered the formation of adhesive ligaments that connected the separating substrates. As the opening of the joint increased, the adhesive ligaments induced extra dissipation through elastic, plastic, and fracture energy; for instance, the elongation strain of the adhesive material specified by the arrows in Fig. 6 was about 74%. Moreover, the snapshots also highlight a relatively large value of the residual thickness (Δ_s^f = 142 μm), despite the fact that the adhesive was already detached from the substrates.

On the other hand, no carbon fibers were involved in the interfacial damage of sanded surfaces, although the exposure of fibers was extensive, as can be observed in Fig. 3. Instead, localized adhesive fibrillation occurred (see the arrows in the corresponding snapshots in Fig. 6) since the adhesive experienced severe peel deformation (the maximum Δ_s recorded during the test was approximately equal to 164 μm). The failed fibrils were seen extensively on the fracture surface of the joint, indicating spots with local cohesive failure, as illustrated by the arrows in Fig. 7. After failure, the stretched adhesive partially relaxed back and a residual thickness as large as Δ_s^f = 145 μm was recorded at the end of the test (last snapshot recorded before catastrophic failure).

The observed differences in the failure mechanisms of the laser-treated (*LC*) and sanded (*S*) interfaces were further analyzed. Schematics of the *LC* and *S* surfaces are shown in Fig. 8(a) along with SEM observations. Due to a thermal interaction between the pulsed CO_2 laser irradiation and the CFRP laminates, only the epoxy resin was removed. Therefore, some fibers had little support or they were already detached from the surface matrix, which can be observed in the *LC* SEM image in Fig. 8(b). Since the exposed fibers were easily detached from the substrate and distributed randomly on the laser-treated CFRP surfaces, diffused interfacial damage occurred at the adhesive/CFRP interfaces, as shown in Fig. 8(c). The loose carbon fibers observed here were largely due to the specific CFRP material employed. Indeed, related previous work [12,15] found that by using pre-pregs with surface resin-rich layers, laser irradiation could be used successfully to generate surface patterns without exposing carbon fibers. On the other hand, sanding removed the epoxy resin and flattened carbon fibers at the same time, and delivered an extremely flat surface. The overall surface was quite homogeneous, *i. e.*, did not display loose fibers, and featured higher surface energy. This enabled larger adhesive deformation and the nucleation of fibrils, thereby leading to a superior mechanical response in the three-point bending tests. However, sanding is neither practical nor viable for the preparation of large and complex surfaces.

3.5. Evaluation of average peel deformation within the adhesive layer

The average peel deformation within the adhesive layer, measured from the snapshots such as those in Fig. 6, is plotted against the normalized displacement δ/δ_{max} in Fig. 9(a) for *PP*, *T*, *LC*, and *S*. The thickness of the adhesive layer Δ_s was obtained by averaging multiple measurements, marked in Fig. 6 by unfilled circles. The deformation was calculated as $(\Delta_s - \Delta_{s0})/\Delta_{s0}$, where Δ_{s0} was the initial thickness of the adhesive layer. As shown in Fig. 9(a), peel-ply-treated and baseline

[1] Fresh epoxy is exposed at the edges of the peel-ply, which provides enhanced adhesion [9].

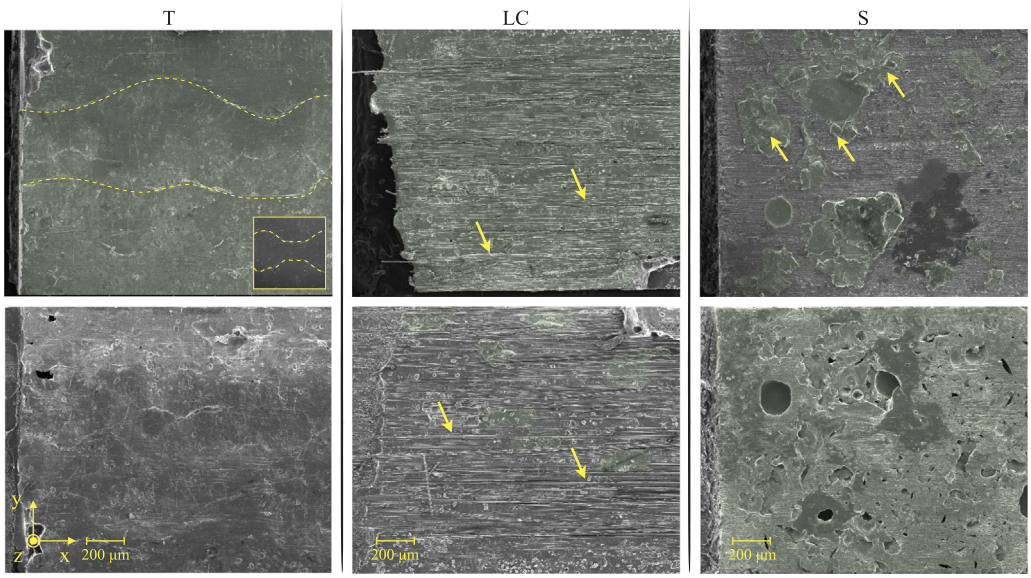

Fig. 7. SEM imaging of fracture surfaces of *T*, *LC*, and *S*. The residues of adhesive on the fracture surfaces are highlighted. Dashed lines depict the imprinted texture of the *T* surface; a similar imprinted texture is also found on the original surface (in the insert). Downward arrows show the loose carbon fibers due to the *LC* surface pretreatment, and upward arrows demonstrate the locations of broken adhesive fibrils on the *S* surfaces. (For interpretation of the references to color in this figure legend, the reader is referred to the web version of this article.)

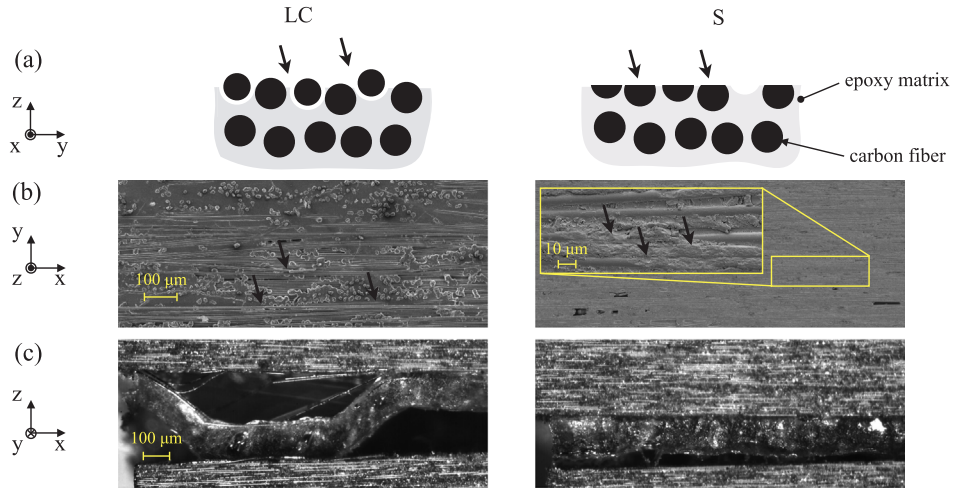

Fig. 8. (a) Surface morphologies and edge damage of the *LC* and *S* surfaces. (b) SEM observations and schematics illustrate the surface configurations after the *LC* and *S* surface pretreatments. The arrows on the *LC* surfaces indicate that part of the carbon fiber is already detached from the surface resin, while the arrows on *S* show the flattened carbon fibers. (c) *In situ* side views of *LC* and *S* reveal different interfacial damage evolution due to the different surface pretreatments. (For interpretation of the references to color in this figure legend, the reader is referred to the web version of this article.)

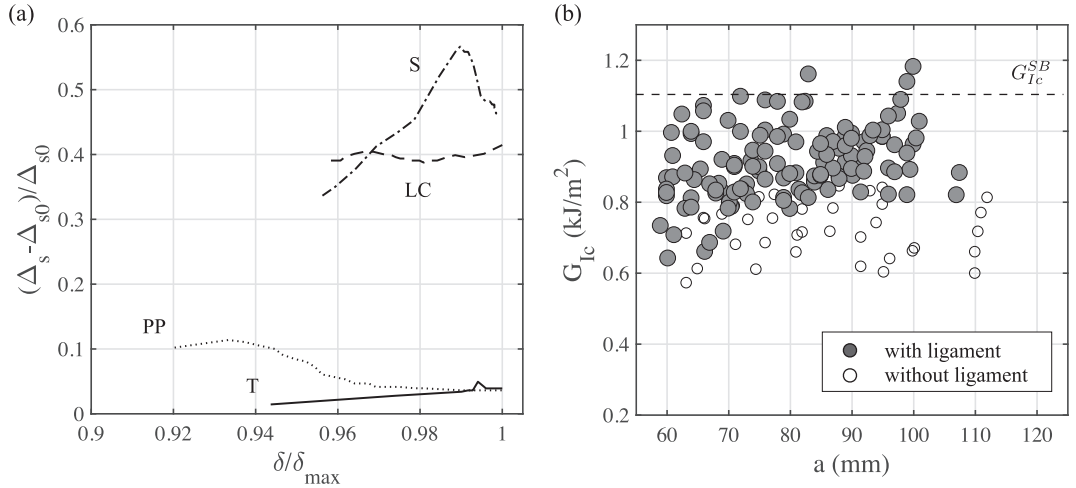

Fig. 9. (a) Average peel deformation $(\Delta_s - \Delta_{s0})/\Delta_{s0}$ versus the normalized global deflection δ/δ_{max} of *PP*, *T*, *LC*, and *S* surfaces. Δ_{s0} is the initial thickness of the adhesive layer, while δ_{max} is the maximum deflection at failure. (b) Fracture toughness of trench-shaped laser-patterned adhesively bonded DCB samples made with the same material employed in this work. The fracture toughness of sandblasting (*SB*) is highlighted with the dashed line. All these toughness results were obtained from the authors' previous work [9].

T specimens displayed limited deformation, which explained the relatively low maximum load recorded during the three-point bending tests. Sanded specimens exhibited the largest deformation just before final failure; the peel deformation reached 56% and then quickly relaxed to 44% after the failure of adhesive fibrils. Although laser-treated specimens experienced diffused interfacial failure, the adhesive layer sustained peel deformation up to 40%. The maximum load recorded during mechanical testing was slightly lower for *LC* than that for sanded surfaces. Although *LC* did not outperform *S*, our previous work suggested that the formation of ligaments could largely enhance the propagation fracture toughness as determined in the DCB tests [9]. Indeed, as indicated in Fig. 9(b), the adhesive ligaments triggered by trench-shaped laser patterns provided an enhanced fracture toughness, as large as that obtained using sandblasting (*SB*). Therefore, the results of *in situ* analyses highlighted that the superior fracture toughness is a result of large tensile deformations sustained by the ligaments before final failure, *i. e.*, deformations as large as 74% were recorded with the current experimental set-up.

4. Conclusions

In this study, the effect of surface pretreatments on the interfacial damage of adhesively bonded CFRP single-lap joints was investigated. The topography of the treated surfaces was assessed using profilometry and scanning electron microscopy. The surface energies and wetting envelopes were obtained using the sessile drop technique and the Owens-Wendt theory. A dedicated test set-up comprised a miniaturized tensile-compression stage and a high-resolution camera was deployed to track the damage *in situ* during three-point bending tests.

It was shown that the load-bearing capability of the joint as well as the evolution of the damage across the interface were strongly correlated with the surface energy. Moreover, the detailed local *in situ* observations demonstrated that the heterogeneous properties of the *LC* surfaces triggered the formation of adhesive ligaments, which underwent significant deformation upon failure. Although this response is strongly material-related (*i. e.*, the pre-pregs in this work were provided with a relatively thin epoxy surface layer), it suggests the potential to achieve improved fracture toughness. However, further investigations are needed to develop tailored surface pretreatments that allow for better controlling the formation of these adhesive ligaments and, in turn, to tailor the joint strength and fracture toughness.

Acknowledgement

The research reported in this publication was supported by funding from King Abdullah University of Science and Technology (KAUST) Office of Sponsored Research (OSR) under award number OSR-2017-CRG6-3388.01.

References

[1] Schmid Fuertes T, Kruse T, Körwien T, Geistbeck M. Bonding of CFRP primary aerospace structures, a discussion of the certification boundary conditions and related technology fields addressing the needs for development. Compos Interfaces 2015;22(8):795–808.
[2] Russell J. Composites affordability initiative: transitioning advanced aerospace technologies through cost and risk reduction. AMMTIAC Quart 2006;1(3):3–6.
[3] Katnam K, Da Silva L, Young T. Bonded repair of composite aircraft structures: a review of scientific challenges and opportunities. Prog Aerosp Sci 2013;61:26–42.
[4] Lu J, Youngblood J. Adhesive bonding of carbon fiber reinforced composite using uv-curing epoxy resin. Compos Part B: Eng 2015;82:221–5.
[5] Heshmati M, Haghani R, Al-Emrani M. Environmental durability of adhesively bonded frp/steel joints in civil engineering applications: state of the art. Compos Part B: Eng 2015;81:259–75.
[6] Korayem A, Li C, Zhang Q, Zhao X, Duan W. Effect of carbon nanotube modified epoxy adhesive on cfrp-to-steel interface. Compos Part B: Eng 2015;79:95–104.
[7] Prolongo S, Gude M, Del Rosario G, Ureña A. Surface pretreatments for composite joints: study of surface profile by SEM image analysis. J Adhes Sci Technol 2010;24(11–12):1855–67.
[8] Holtmannspötter J, Czarnecki J, Wetzel M, Dolderer D, Eisenschink C. The use of peel ply as a method to create reproduceable but contaminated surfaces for structural adhesive bonding of carbon fiber reinforced plastics. J Adhes 2013;89(2):96–110.
[9] Tao R, Alfano M, Lubineau G. Laser-based surface patterning of composite plates for improved secondary adhesive bonding. Compos Part A: Appl Sci Manuf 2018;109:84–94.
[10] Hartwig A, Vit G, Dieckhoff S, Hennemann O. Surface treatment of an epoxy resin by CO_2 laser irradiation. Die Angew Makromol Chem 1996;238:177–89.
[11] Bénard Q, Fois M, Grisel M, Laurens P. Surface treatment of carbon/epoxy and glass/epoxy composites with an excimer laser beam. Int J Adhes Adhes 2006;26(7):543–9.
[12] Palmieri F, Hopkins J, Wohl C, Lin Y, Connell J, Belcher M, et al. Laser surface preparation of epoxy composites for secondary bonding: optimization of ablation depth.
[13] Kruse T, Koerwin T, Heckner S, Geistbeck M. Bonding of CFRP primary aerospace structures - crackstoppings in composite bonded joints under fatigue. ICCM 20 20th international conference on composite materials (July). 2015. p. 19–24.
[14] Kreling S, Fischer F, Delmdahl R, Gäbler F, Dilger K. Analytical characterization of cfrp laser treated by excimer laser radiation. Phys Procedia 2013;41:282–90.
[15] Palmieri F, Belcher M, Wohl C, Blohowiak K, Connell J. Laser ablation surface preparation for adhesive bonding of carbon fiber reinforced epoxy composites. Int J Adhes Adhes 2016;68:95–101.
[16] Yokozeki T, Ishibashi M, Kobayashi Y, Shamoto H, Iwahori Y. Evaluation of adhesively bonded joint strength of cfrp with laser treatment. Adv Compos Mater 2016;25(4):317–27.
[17] Almuhammadi K, Selvakumaran L, Alfano M, Yang Y, Bera T, Lubineau G. Laser-based surface preparation of composite laminates leads to improved electrodes for electrical measurements. Appl Surf Sci 2015;359:388–97.
[18] Fischer F, Kreling S, Dilger K. Laser surface pre-treatment of carbon fiber-reinforced plastics (CFRPs) for adhesive bonding. Laser surface modification and adhesion. 2014. p. 103–38.
[19] Reitz V, Meinhard D, Ruck S, Riegel H, Knoblauch V. A comparison of ir- and uv-laser pretreatment to increase the bonding strength of adhesively joined aluminum/cfrp components. Compos Part A: Appl Sci Manuf 2017;96:18–27.
[20] Moradi A, Carrère N, Leguillon D, Martin E, Cognard J. Strength prediction of bonded assemblies using a coupled criterion under elastic assumptions: effect of material and geometrical parameters. Int J Adhes Adhes 2013;47:73–82.
[21] Tang J, Sridhar I, Srikanth N. Nondimensional analysis of single lap joint subjected to out-of-plane loading. Int J Solids Struct 2015;62:229–38.
[22] O'Dwyer D, O'Dowd N, McCarthy C. In-situ sem mechanical testing of miniature bonded joints. Int J Adhes Adhes 2014;50:57–64.
[23] Adams RD. Adhesive bonding: science, technology and applications. Elsevier; 2005.
[24] Rudawska A. Selected aspects of the effect of mechanical treatment on surface roughness and adhesive joint strength of steel sheets. Int J Adhes Adhes 2014;50:235–43.
[25] Budhe S, Ghumatkar A, Birajdar N, Banea M. Effect of surface roughness using different adherend materials on the adhesive bond strength. Appl Adhes Sci 2015;3(1):20.